Optics and Lasers in Engineering 173 (2024) 107919

Contents lists available at ScienceDirect

Optics and Lasers in Engineering

journal homepage: www.elsevier.com/locate/optlaseng

Structural thermal optical performance (STOP) analysis and experimental verification of an hyperspectral imager for the HYPSO CubeSat

Fermin Navarro-Medina [a,*], Adriënne Esmeralda Oudijk [b], Marie Bøe Henriksen [b], Uxia Garcia-Luis [a], Alejandro Gomez-San Juan [a], Tor Arne Johansen [b]

[a] AtlanTTic, Universidade de Vigo, Escola de Enxeñaría Aeronáutica e do Espazo, Aerospace Technology Research Group, 32004, Ourense, Spain
[b] Department of Engineering Cybernetics, Norwegian University of Science and Technology, Trondheim 7034, Norway

ARTICLE INFO

Keywords:
Thermo-elastic analysis
STOP analysis
Hyperspectral camera
Thermo-structural model
Optical model

ABSTRACT

The evaluation of space optical instruments under thermo-elastic loads is a complex and multidisciplinary process that requires integrating thermal, structural, and optical disciplines. This thorough analysis often requires substantial resources, leading small satellite projects to exclude it from their schedules. However, even though the instrument discussed in this paper is compact, its complex design and stringent dimensional stability requirements demand a comprehensive evaluation of its performance under thermal loads. The hyperspectral camera, which comprises 18 lenses, a grating, a slit, and a detector, is especially vulnerable to thermo-elastic distortions, as the deformation of even a single lens could significantly impact its performance. In this paper, we present the experimental validation of the STOP analysis applied to the HYPerspectral Small satellite for ocean Observation (HYPSO) Hypespectral Imager (HSI) model. Both the HSI Structural Thermal Optical Performance (STOP) numerical model and the HSI engineering model were subjected to identical thermal conditions in the simulations and in a Thermal and Vacuum Chamber (TVAC), and subsequently the optical results derived from simulations and the test campaign compared. To characterize the thermal field, an infrared camera and thermocouples were used. Moreover, to assess the thermal performance of the HSI, we measured the Full Width at Half Maximum (FWHM) of the main peaks in the intensity-wavelength spectra when the hyperspectral camera targeted a known spectral lamp. After individually calibrating the STOP models so that the FWHM and index of the intensity peaks are in close alignment with the experimentally measured FWHM and index, the lenses most sensitive for displacements were characterized.

1. Introduction

1.1. STOP analysis of space-based optics instruments

Performing STOP analysis has gained considerable attention in recent years. While numerous studies have been conducted, either partially or completely, the involvement of multiple disciplines, software interfaces, and space actors presents significant challenges in obtaining accurate and precise results, even for a single spacecraft instrument. Typically, the engineering team responsible for platform design characterizes the primary structural and thermal control subsystems. However, it is common to find payloads which have their own structure and, poten- tially, dedicated thermal control hardware. Examples of such payloads include space telescopes or cameras, whose optical performance has been greatly influenced by temperature gradients over time and space (within a single component) since the early days of optical instruments in space exploration. Thermo-elastic deformations play a crucial role in introducing performance errors in space-based telescopes or cameras, impacting the efficiency not only of astronomical devices but also Earth observation telescopes, communication systems [1,2], and any system that requires dimensional stability in the space environment [3].

Developing a comprehensive STOP analysis is a challenging and multidisciplinary task. Temperature variations induce structural deformations which in turn cause optical performance errors [4]. This process involves three sequential analyses, each employing a different numerical approach and often managed by separate teams dedicated to the thermal, structural, and optical matters. The lack of communication between these teams can lead to errors and inefficiencies, which are further intensified by the absence of a unified mathematical framework

* Corresponding author.
E-mail address: fermin.navarro.medina@uvigo.es (F. Navarro-Medina).

https://doi.org/10.1016/j.optlaseng.2023.107919
Received 19 July 2023; Received in revised form 20 September 2023; Accepted 26 October 2023
Available online 6 November 2023

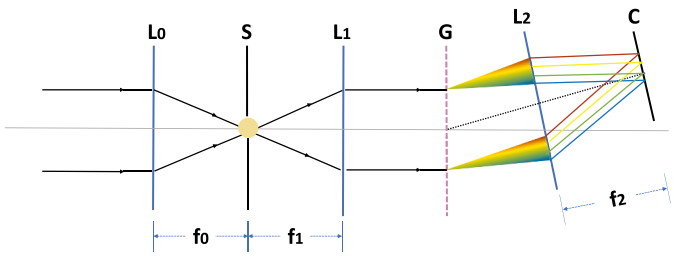

Fig. 1. The optical diagram of the HYPSO-1 spectrograph consisting of a focusing front lens (L_0), an entrance slit (S), a collimator (L_1), a 300 grooves/mm transmission grating (G), a focusing lens (L_2) and a sensor (C).

for thermo-elastic analyses in the space industry. The European Space Agency (ESA) has taken steps towards standardization by promoting the use of an uniform software across its mis- sions, namely ESATAN for thermal analysis, NASTRAN for structural analysis, and primarily relying on two optical analysis software packages: Zemax and CodeV.

One of the main complexities in performing these analysis arises from the requirement to map temperatures from the Thermal Mathematical Model (TMM) to the Finite Element Model (FEM), which typically has a significantly larger number of nodes (at least, one order of magnitude higher). Ad- ditionally, the modelling approach for different features tends to differ. For instance, in thermal analysis, conductive interfaces are often used to model structural connections, while structural models commonly employ rigid body constraints to represent its behaviour. Regarding the thermo-elastic analysis, ESA has invested considerable effort in standardizing the thermo-structural interface in space-based systems. In pursuit of this objective, ESA promoted the employment of Sinas for performing thermal mapping. It is a software package developed by ESA that was made publicly available, using the Prescribed Average Temperature (PAT) method, which gives the best correlated results until date [5].

Moreover, it is crucial to accurately model the thermo-elastic deformation mechanisms. Electronic boards serve as example, where different modelling approaches are employed. Typically, these components are represented by Non-Geometrical Thermal Node (NGTN) and their associated dissipation in thermal analysis, while being treated as lumped masses in structural analysis. However, this simplified modelling technique may not adequately capture the stiffness interaction with the surrounding structure. In thermo-elastic analysis, it is frequently necessary to model the electronic board as a shell structure.

ESA has recently published the European Guidelines for Thermo-Elastic Verification [6], a the result of the progress achieved by the European working group for thermo-elastic analysis (to which some of the authors of this paper belong). This further reinforces the relevance of accurately predicting these deformations, particularly for applications with stringent dimensional requirements. Furthermore, there is a dedicated working group to address aspects related to not only thermo-elastic analysis but also the complete STOP chain.

The James Webb Space Telescope (JWST) mission serves as example of a complete STOP analysis, which accurately pre- dicts thermo-elastic distortion and optical performance, including a sensitivity study to assess modelling uncertainties [7]. Another relevant contribution for a complete STOP analysis is pre- sented in [8], where NX Space Systems Thermal, NASTRAN, and Matlab were used for the thermal, structural, and optical models, respectively. The study highlights two primary challenges in the thermo-elastic problem. Firstly, using the nearest node method to interpolate temperatures in the structural model from the thermal model resulted in artificial thermal gradients. Secondly, conducting such a multi-disciplinary analysis needs the integration of different software packages to streamline data exchange methods between models, often relying on one-time use codes or manual procedures.

Despite numerous efforts to streamline the STOP analysis process, many space projects still require the execution of three separate studies. Consequently, in cases where researchers detect optical performance losses at the end of the STOP analysis chain, identifying and tracing them back to the primary cause can be labour-intensive or even impossible. Examples such as the Hubble Space Telescope (HST) or Gaia have shown that thermo-elastic effects can become evident once in orbit [4]. Enhancing the overall STOP analysis can be achieved by establishing a unified approach to develop the analysis chain, taking into account the specific requirements of each field involved and the final system being evaluated.

This paper highlights selected efforts made within the STOP chain. For instance, in [9], the authors created a structural model using NASTRAN to evaluate node displacements and rotations in the optics. In [10], ray-tracing was employed to model the optical performance of a specular reflective baffle for the High spatial Resolution Imaging Camera (HRIC) telescope in the BepiColombo spacecraft, on its mission to Mercury. The thermo-elastic deformation was calculated using a NASTRAN structural model, with mirror geometry represented by straight lines and Bezier splines, and the displacement of reference points used to deform the mirror shapes. In [11], the thermal and structural models of BepiColombo's HRIC telescope are outlined, including the calculation of piston-tilt movements of the mirrors, inducing optical aberrations and deviations in the peak ray intensity from the sensor's centre. They conclude that the thermal deformation error is negligible as the deviation is smaller than the pixel size. Lastly, [12] presents a study focused on the final stage of the STOP analysis chain, where the optical design of a reflecting telescope for CubeSats is accomplished using Optics Studio.

The space environment is known for its harsh and variable thermal conditions, leading to significant spatial and temporal temperature gradients within space structures, ranging from tens to hundreds of degrees Celsius [13]. While the impact of Coefficient of Thermal Expansion (CTE) on several spacecraft components has been well-documented (e.g., solar panel booms in [14] or large frame- and truss-type space structures in [15]), there is a limited availability of studies focusing on optical instruments. One exception is [16], where a structural model and ray tracing simulation of the THESEUS SXI instrument in the McXtrace framework were conducted. The analysis found no distortion in the Point Spread Function (PSF) merit figure for the applied thermal load cases. However, it is worth noting that the thermal cases were arbitrarily selected and not derived from any instrument-specific thermal model.

1.2. *HYPSO HSI instrument*

In this paper, we present not only the thermal, structural, and optical models, but also the results of an experimental verification campaign applied to HYPSO HSI model. The HYPSO mission, is an initiative lead by the Norwegian University of Science and Technology (NTNU), which aims to monitor ocean colour. The HSI on the HYPSO-1 CubeSat (see Fig. 1) is a hyperspectral instrument covering visible to near-infrared wavelengths (from 400 to 800 nm), which has a theoretical FWHM of 3.33 nm and a measured FWHM of 5 nm from in flight measurements [17–20], which is a key performance parameter for the instrument. The same instrument is also planned for use on the subsequent series (as HYPSO-2, for instance), which is under development and scheduled for launch in 2024.

The validation and verification of the results presented in this paper were carried out through rigorous testing activities, constituting a pivotal milestone in the development of instrumental optical research onboard small platforms. The initial stage of these testing initiative needs the determination of the required accuracy, taking into account the allowable limits of key metrics essential to mission performance, such as the maximum relative displacements between components of an optical bench. Alternatively or complementary to tests (depending of project time constraints), the uncertainty of results from uncertainty analysis should be established to ensure that the simulation outputs

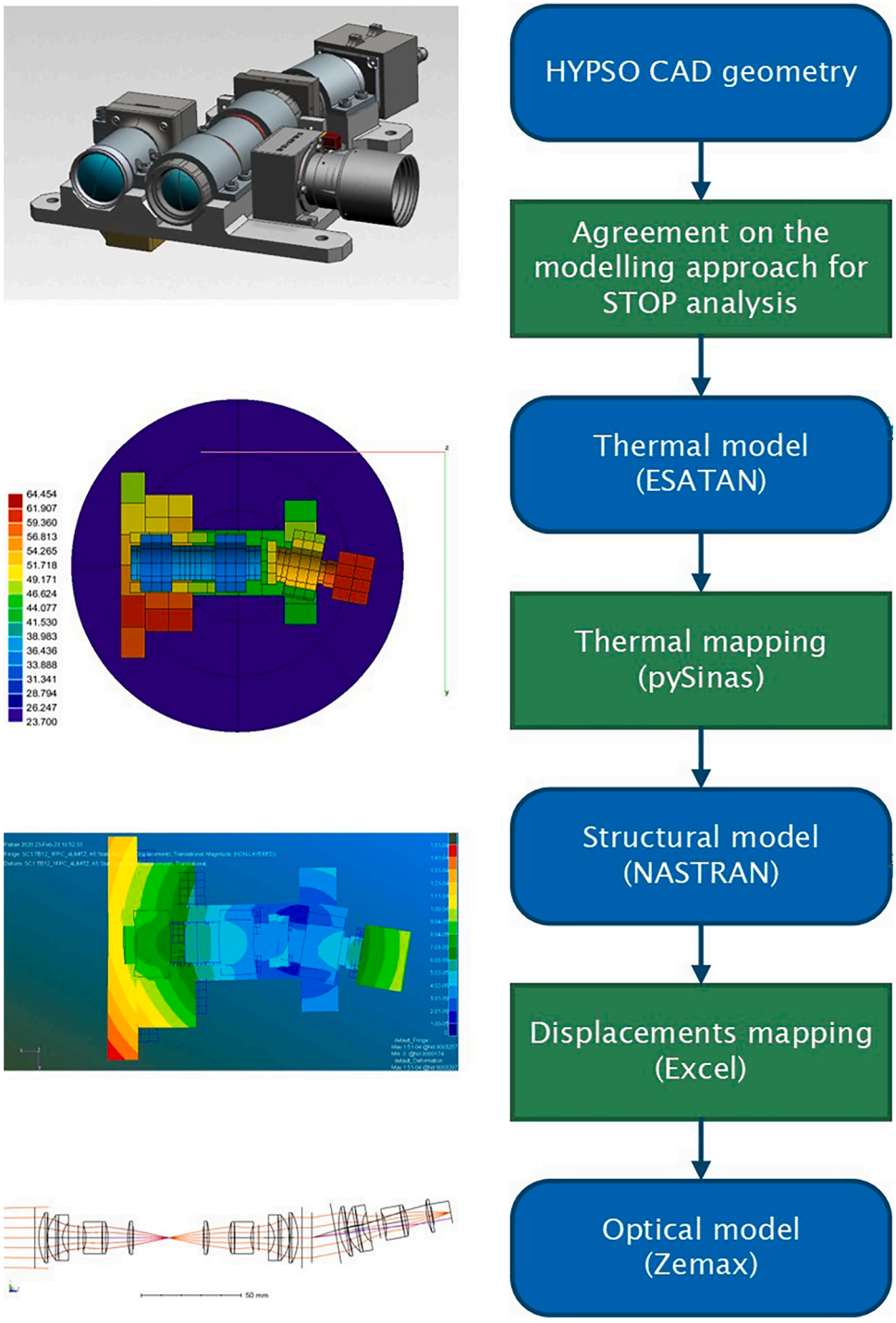

Fig. 2. Scheme of the STOP analysis software applied to HYPSO HSI.

comply with the acceptable ranges determined by the performance engineering team. Given the precision, pointing, and tracking requirements, it is imperative that the testing techniques employed are characterized by consequent accuracy and non-intrusiveness.

We subjected both the HSI STOP numerical model and the HSI engineering model (in the TVAC) to identical thermal loads, to compare the optical outputs from simulations with those derived from the test campaign. To measure the thermal loads, we employed an infrared camera and several thermocouples. The thermal performance of the HSI was determined using the FWHM and the index of the main peak in the intensity-wavelength spectra when the hyperspectral camera points at a known spectral lamp (with Argon gas used as the reference). The STOP numerical model is set up such that the single-peaks of the Argon lamp would match with the experimental findings. A review of analogous tests was conducted to enhance our un- derstanding of the system conditions.

In [21], an experimental correlation was conducted to vali- date a thermal model of a spacecraft structure for thermo-elastic analysis. This correlation involved the use of an infrared camera and thermocouple sensors. A specific thermo-elastic test demonstrator was employed, with the non-black outer surfaces covered with black tape to be better captured by the camera. Heater lines were used to establish varying thermal gradients on the test item. Although their thermal model correlated well with thermocouple sensors at a given point, it proved insufficiently detailed to simulate large thermal gradients observed by

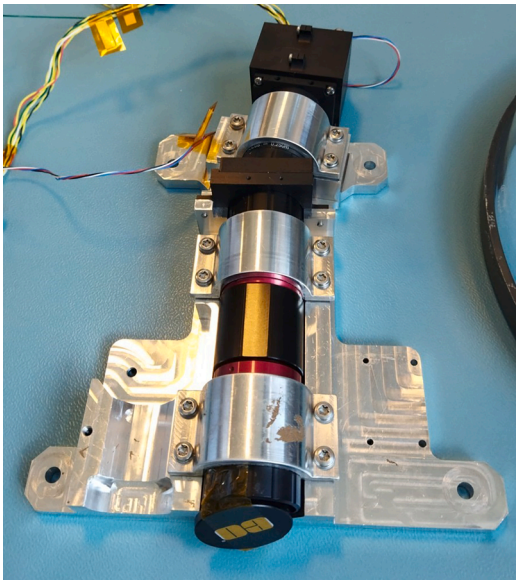

Fig. 3. Picture from the top side of the HSI.

the infrared camera. However, refinement of the thermal mesh in ESATAN improved the correlation of the thermal model. Errors were quantified and categorized into (a) camera and temperature measurement inaccuracies, and (b) post-processing of infrared images and spatial mapping of the thermal model.

Moreover, experimental testing has been conducted on payloads similar to ours; however, these were not specifically aimed at verifying the thermo-elastic response. In [22], the measurement of the PSF for characterizing the co-registration and resolution of two commercial hyperspectral cameras similar to ours are tested. Their results provide valuable insights into the hyperspectral camera itself, but the tests were not conducted under space conditions.

Most of the missions analysed above are primarily for medium or large spacecraft, but small satellite programs sel- dom incorporate thermo-elastic analysis in their schedules due to budget constraints and their short lead time. Only partial studies of the root disciplines (thermal control, structures, and optics) are available in the literature. The impact of heat sources on optical instruments is investigated in [23,24], and [25]. An analytical study of thermal effects in CubeSats is found in [26]; a comparison of different paints in small satellites in [27]; and the thermo-electric modelling of small satellites in [28]. NTNU's previous thermal characterization on the hyperspectral camera is found in [29]. However, a comprehensive model of the heat impact on the HSI has yet to be identified, which is the focus of this paper.

This paper is organized as follows: in Section 2, a overview of the STOP analysis applied to the hyperspectral camera is presented. In Sections 3, 4, and 5, the thermal, the structural, and the optical models are presented, respectively. In Section 6, the experimental set-up is sum-up. Finally, in Sections 7 and 8 the results and conclusions are outlined.

2. Overview of the STOP method used

In the introduction, we acknowledged several partial or complete STOP studies conducted previously. As above-mentioned, complete STOP analysis are out of the scope of many space optical payloads design. One of the main factors is the complexity of combining such different disciplines within only one work- ing team, while separated teams are used to lack of providing efficient information exchange in between. The consequence is that only large space missions are able to afford the development of thermal, structural, and optical analysis of their optical instruments in an integrated sequence. Despite numerous efforts to streamline the STOP analysis process, many space projects still require the execution of three separate studies. Consequently, in cases where researchers detect optical performance losses at the end of the STOP analysis chain, identifying and tracing them back to the primary cause can be labour-intensive or even impossible. Examples such as the HST or Gaia have shown that thermo-elastic effects can become evident once in orbit [4]. Enhancing the overall STOP analysis can be achieved by establishing a unified approach to develop the analysis chain, taking into account the specific requirements of each field involved and the final system being evaluated.

The present study diverges from those by providing a comprehensive evaluation using the software reference in ESA-led projects for each of the disciplines involved, as depicted in Fig. 2. Our focus is on the optical instrument, a hyperspectral imager HSI, located within the CubeSat HYPSO, [30]. To discern the temperature distribution, we constructed a thermal model of the HSI in ESATAN. In the space thermal control discipline, thermal models of payloads and their environment are aimed to determine the temperatures of key components, and assure they are inside required ranges, by means of thermal control hardware. However, thermal models dedicated to STOP analysis focus on capture temperatures but also thermal gradients where displacements and stresses may impact the op- tical performance of the instrument. The mapping of the results from the thermal mesh to the structural one was facilitated using pySinas, the Sinas python extension. It should be pointed out that the difference in one order of magnitude between the number of nodes in thermal models and thermal finite element models, as well as the node typology difference, requires a consistent conversion process. It implies that structural elements corresponding to one specific thermal node are correlated in terms of averaged temperatures and heat fluxes with adjacent nodes. This in itself and its implementation in a payload for a small satellite space project represents a major challenge achieved. NASTRAN was used for developing a structural model to ascertain the displacements. We designed a custom structural-optical interface application in Excel and finally built an optical model with OpticStudio (from Zemax) to obtain the optical parameters of the HSI. The in-house development of an interface between the structural and optical model is also a challenge achieved in this work. Some commercial soft- ware like SigFit is adopted to calculate surface deformation and stresses due to thermal loads, when linking structural and optical models. However, the large number of optical elements con- tained in our HSI lead us to develop our own structural-optical interface.

3. Thermal model

The thermal model was conceived based on the engineering model of the HSI for the HYPSO-1 mission, [30]. This engineering model is almost identical to the flight model, assembled on an identical platform but without the Red-Green- Blue (RGB) camera installed. The primary focus of the thermal model is on the hyperspectral camera configured for tests within a TVAC, which is described in this section.

3.1. Thermal requirements

A critical initial step was to review the thermal requirements of the HSI, determining if the thermal model requires special considerations to account for temperatures or heat fluxes at par- ticular locations. Upper operational and non-operational temperature limits were set at 50 °C and 60 °C, respectively. These limits guided the numerical simulations and experimental campaigns to safeguard the thermal integrity of the camera. The HSI thermal design is based in passive elements, allowing for suitable equilibrium temperatures for all relevant thermal cases that might take place in orbit. Amongst the passive elements incorporated in the HSI they were the thermo-optical properties of machined aluminium. Moreover, there is a set of four insu- lating dampers which, apart from their structural function, act to limit heat conduction from the CubeSat structure to the HSI platform.

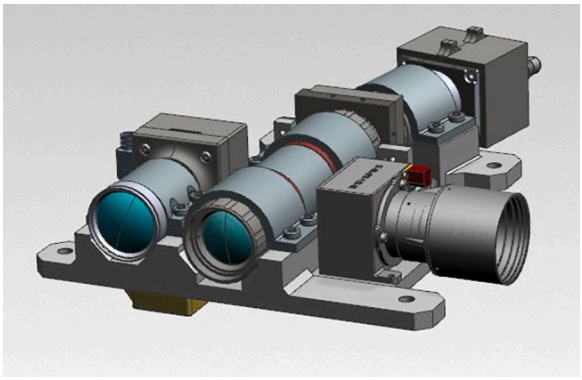

Fig. 4. Engineering model version of HSI mechanical design given as Computer-Aided Design (CAD) model. RGB (left) and the star tracker (right) also included.

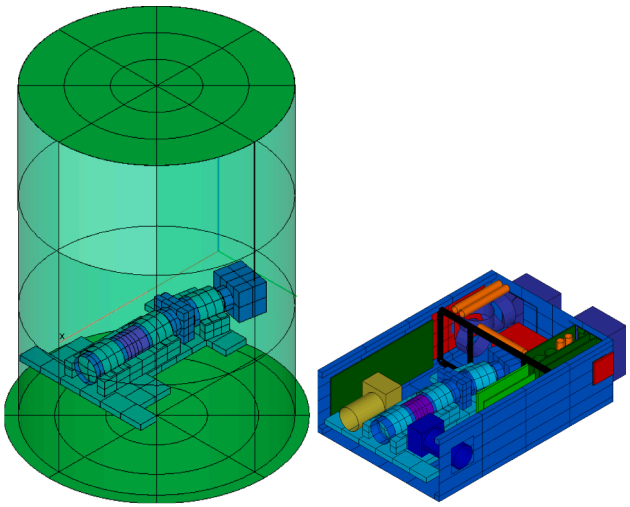

(a) TVAC (b) HYPSO

Fig. 5. Thermal model for (a) TVAC tests and for (b) in-orbit simulations.

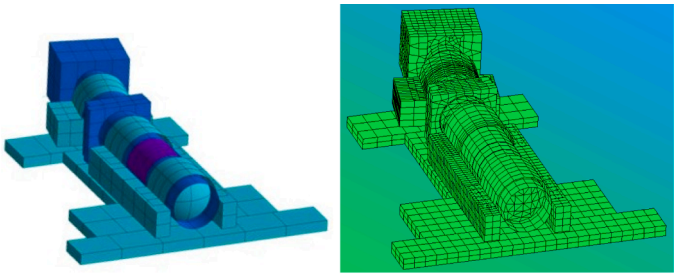

(a) Thermal mesh (b) Structural mesh

Fig. 6. Discretization of the (a) thermal mesh with low detail in ESATAN and (b) refined in NASTRAN.

3.2. Mechanical design considerations for the thermal model

There are several mechanical design aspects which have significant implications for thermal modelling. A picture of the HSI engineering model is shown in Fig. 3.

We generated a CAD model of the HSI flight model (Fig. 4) using CATIA V5, which provided a common baseline for thermal, structural,

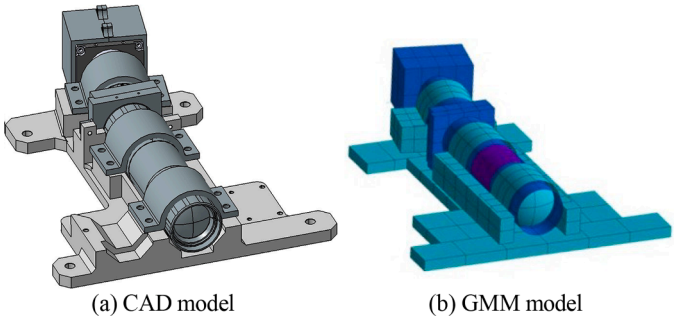

(a) CAD model (b) GMM model

Fig. 7. Comparison of the (a) CAD model (made in CATIA) and (b) GMM (made in ESATAN).

and optical models, facilitating the interaction between teams towards determining the final configuration. Engineers responsible for the thermo-elastic evaluation chose to exclude the RGB (left side) and the star tracker (right side) during the TVAC test campaign to prevent potential damage on the instruments. It is crucial to account for the thermal influence of these elements and other dissipation sources close to the hyperspectral camera on the HYPSO flight thermal model. However, the comprehensive STOP method is applied solely to the HSI engineering model, which is suitable for TVAC testing.

There are several design differences between the engineering and flight model of HYPSO-1 (which is currently in-orbit, operated by the HYPSO team at NTNU). A key factor affecting the thermal design is that the flight model includes a strap between the detector box and the HSI platform, not present in the engineering model. This variation could lead to differences in thermal conduction paths within the HSI, which could be relevant if a comparison between the two models is to be established.

Real thermal load cases are heavily influenced by the Cube- Sat's orbital environment and the power dissipation loads proximate to the HSI. However, the developed thermal model's primary objective is for thermo-elastic verification under TVAC conditions, and thus it has been analysed within this specific thermal environment. Given the lack of a complete thermal control during testing (no cooling system is present), room tem- perature serves as the reference load case. Furthermore, we employ the temperature field when the heater load is stabilized at several levels to establish different steady-state conditions dur- ing the analysis of the optical thermo-elastic performance for hot case scenarios.

This demands the creation of two different thermal models for the evaluation of in-orbit and TVAC performance. As such, we have developed two separate thermal models, each enveloped by either the CubeSat or the TVAC, to establish unique boundary conditions (see Fig. 5). In this initial phase of the HSI characterization, our focus is predominantly on the TVAC thermal model.

3.3. Thermo-elastic analysis considerations for the thermal model

Thermal models employed for thermo-elastic analysis differ significantly from those used for thermal control objectives. A primary distinction is that thermal control analysis aims to identify the temperatures in the most important components of the Device Under Study (DUS), whereas a thermo-elastic nu- merical model must represent the thermo-elastic deformation mechanisms accurately. This typically requires a more detailed model to capture the thermal gradients across the DUS.

The hyperspectral imager onboard HYPSO operates optimally within a moderate temperature range. However, even if the instrument's temperature remains within the allowable operational ranges set by the HSI components manufacturers, the optical performance of the camera could still be affected. The variability of the thermal environment could induce spatial and temporal deformation changes across the HSI.

In response to this challenge, we have adopted an approach to

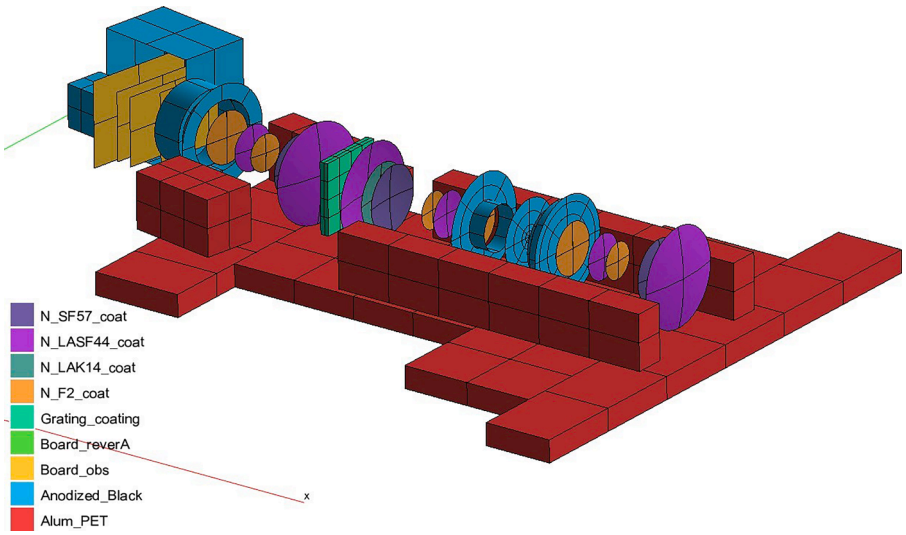

Fig. 8. Thermo-optical properties of the GMM surfaces.

Table 1
Values of the thermo-optical properties (from [31] and [32]).

Thermo-optical property	Infra-red emissivity	Infra-red transmitivity
Optical glass	0.07	0.93
G116 reverse A	0.89	0.0
G116 obverse	0.86	0.0
Anodized black	0.89	0.0
Bare Aluminium	0.035	0.0
Glass B270	0.081	0.919
N-F2 coat	0.003	0.997
N-LAK14 coat	0.002	0.998
N-SF57 coat	0.009	0.991
N-LASF44 coat	0.002	0.998

creating thermal and structural numerical models jointly. This allows us to identify each discipline's specific requirements and tackle the thermo-elastic problem in-depth (Fig. 6).

3.4. Geometrical mathematical model

Developing the thermal model involves two steps: (a) creat- ing the Geometrical Mathematical Model (GMM) (discussed in this subsection), and (b) the TMM (detailed in Section 3.5). The GMM draws upon the geometric details of the HSI internal and external components as depicted in the CAD model. Fig. 7 presents an external view of both the HSI CAD model and the GMM. It is important to note that the GMM is designed to represent surfaces that are significant for the calculation of radiative heat exchange, thus including only those with a large area. However, for a thermo-elastic thermal model, it is often advisable to incorporate additional elements, such as brackets, which, despite being unnecessary for characterizing the radiative environment, their inclusion can enhance the accuracy of computed thermal deformations in the structural model. The different components of the HSI GMM are classified into six hierarchical items in a 1000-nodes model: Front Objective (FOB), Slit Assembly (SLA), Collimator Objective (COB), Grating Assembly (GRA), Detector Objective (DOB), and Detector Box (DET).

The radiative heat exchange between the surfaces of the GMM depends on the mutual field of view and their thermo-optical properties. The properties used for the thermal model are displayed in Fig. 8. Furthermore, the values for infrared emissivity and solar absorptance are detailed in Table 1.

3.5. Thermal mathematical model (TMM)

The TMM involves the definition of bulk materials, the conductive connections between nodes, the power dissipation within components,

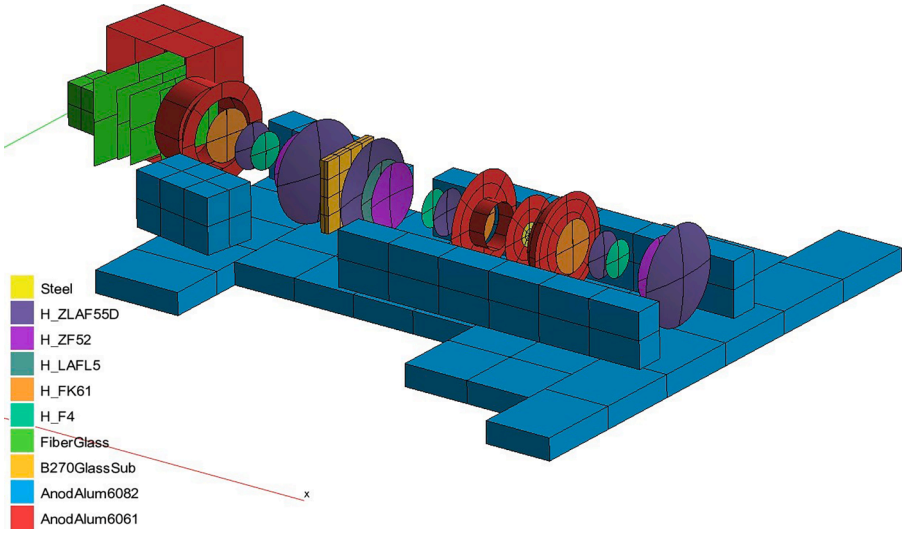

Fig. 9. Bulk properties of HSI elements.

Table 2
Values of bulk properties (from [31] and [32]).

bulk property	density [kg/m^3]	specific heat [$j/(kg \cdot k)$]	thermal conductivity [$w/(m \cdot k)$]
fibre glass	2540	787	1.1
Steel	4600	525	22.15
Aluminium 6061	2770	896	167
Aluminium 6082	2770	896	170
Glass B270	2550	800	1
Optical glass	2560	800	1
H-LAFL5	3630	630	0.89
H-ZF52	3530	660	0.99
H-F4	2650	810	1.05
H-ZLAF55D	4440	530	0.82
H-FK61	2650	810	1.05

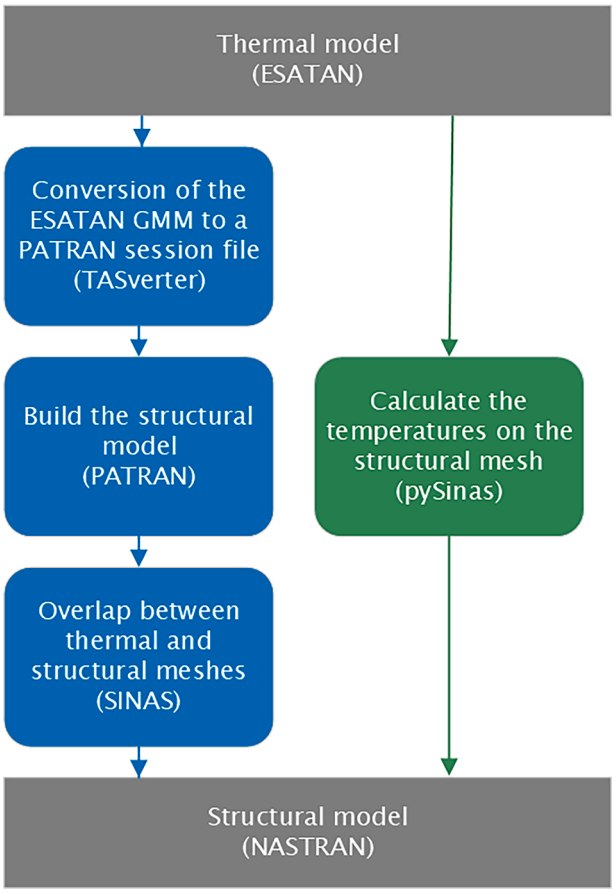

Fig. 10. Modelling process in the thermal-structural interface.

the establishment of analysis cases, and the calculation of temperatures and heat fluxes for each ther- mal scenario. The bulk materials used are represented in Fig. 9, and the thermal property values are given in Table 2. The materials listed in Table 2 are used (a) by ESATAN for computing thermal conduction through the materials of the modelled geometry, and (b) by the thermal engineer for calculating linear conductors between geometries not depicted in the GMM.

Geometric links (Linear Conductors (GLs)) between shells connected via elements which lack of a physical representation in the GMM must be manually calculated (in this model, they were over 250 linear conductors). It is important to highlight that linear conductor calculations constitute one of the primary sources of uncertainty in a TMM. Hence, it is necessary to evaluate their implications through either an uncertainty analysis or a test validation, to ensure confidence in the computed values. In this paper, we opt for performing tests (as described in section 6). The upcoming paragraphs detail the different types of computed linear conductors.

To determine the conductive interface of different structural subparts belonging to the same machined part, a fused GL is defined, accounting for only the conductive resistance across the materials. For instance, the thermal resistance between the baseplate and the bracket's upward extensions were evaluated using this method. Some structural connections also have a contact resistance (i.e., brackets to platform), so a contact conductance is added to the GL in these cases. For interfaces where good contact occurs between two surfaces (potentially, due to the pressure applied by a tightened screw), we adopt a con- tact conductance of 500 W/m^2K, following the recommendations given in [31]. Alternatively, the contact conductance in the screw teeth is modelled as 300 W/m^2K. Lastly, some linear conductors need to be defined to quantify the heat transfer through electrical connectors, which are transferred through pinned connectors for the power supply and the ethernet cable. In all cases, the dimensions for computing the GL are extracted from the HSI CAD model.

Internal heat exchange arises due to external and internal heat sources. For an orbiting spacecraft, external sources include solar, albedo and planet fluxes, while internal sources involve the power consumption of electronic components. In this thermal model, the HSI's external environment will be the TVAC's glass dome and bottom baseplate, which maintain room temperature throughout the tests. The TVAC also has a heating system with a maximum power of 127.5 W within the vacuum chamber, which will be employed to increase the temperature of the HSI platform with respect to the reference thermal balance case without heating power. Heat dissipation from the HSI, with a value of approximately 2.7 W, occurs at the detector/sensor at the end of the optical path, which is the optical surface C in Fig. 1. The heat dissipation from the light source located approximately 30 cm from the wall chamber window is also incorporated into the model, due to its effect on the test's thermal environment.

4. Structural model

The second step in the STOP analysis sequence involves conducting a structural study. Future structural analyses on HYPSO could provide valuable insights into the satellite's mechanical performance under launch loads (like static, vibration, random, or shock simulations). However, the objective of this model deviates significantly from that. Instead, our goal is to determine the thermal stress and displacements of the HSI, which can then serve as inputs for the optical model in Zemax, and subsequently, enable the calculation of deviation in performance of the most relevant optical parameters. The subsequent subsections delve into the modelling process for the thermo- structural interface and the structural model itself.

4.1. Modelling process of the thermo-structural interface

The structural model for the thermo-elastic investigation is not independent entity; rather, it has been developed from the outset to maintain comprehensive correlation with the thermal model (as illustrated in Fig. 10). This correlation stems from using the GMM as the foundation for constructing the structural mathematical model. The thermal model is exported in the STEP-TAS format and converted into a PATRAN session file using TASVerter (an ESA software tool). Even with the work done in the GMM using ESATAN, several operations are necessary, mainly involving cutting surfaces with holes using boolean operations and adjusting intersections which are not fully coincident. Following a successful import into PATRAN, the structural mesh is derived from the thermal GMM, increasing the level of detail and converting the lumped volumes into finite elements.

The next step involves using Sinas for overlapping the ther- mal and structural meshes. It is advisable to initially break down both models into smaller groups for sequential overlapping, to avoid mismatches

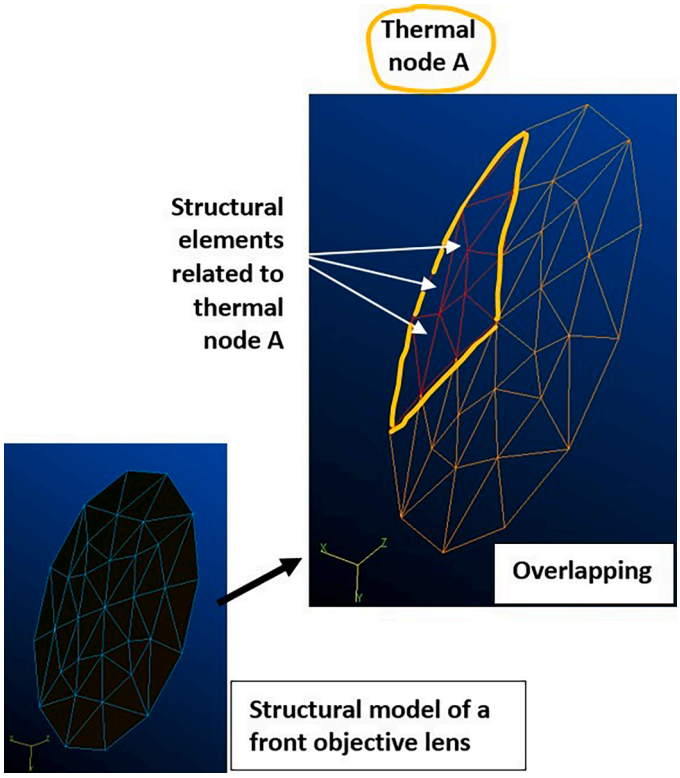

Fig. 11. Example of overlapping between large thermal nodes and small structural elements in the lenses of one of the HSI objectives.

Table 3
Structural analysis checks for the thermo-elastic study.

Structural check	Objective	Expected results
Geometrical correspondence	To identify any significant discrepancies between thethermal and structural geometries that might prevent en- gineers from establishing the thermal load conditions necessary for deformation evaluations.	Complete or near-complete alignment be- tween the GMM and the structural geometry.
Standard structural checks	Verification of free nodes, free edges, element coinci- dence, element shrinkage, element distortion, rigid ele- ments, and material properties.	Correct modelling of all elements with a good mesh quality.
Rigid body frequency check	To derive the primary frequencies of the solid normal modes in the lack of boundaries and loads.	The initial six frequencies shall be below 0.005 Hz and the subsequent frequencies must be in the order of hundreds.
Stress-free isothermal expansion	To confirm that the structural model does not retain resid- ual thermal stresses. Apply an Aluminium Alloy material to the entire structure and increase the temperature by 100 K.	The Von Misses thermal stresses should be lower than 0.01 MPa.

between elements that belong to different parts. Yet, in the first overlap iteration, it is common to identify structural elements that do not correspond to any thermal node, or even elements that overlap with two or more thermal nodes, leading to unclear thermal-structural corre- spondence. During this phase, engineers often need to review and manually identify certain correspondences between elements. Fig. 11 depicts an example of multiple structural nodes asso- ciated with larger thermal nodes.

Table 4
Structural analysis reference cases for the thermo-elastic study.

Structural reference case	Test case objective and thermal load conditions	Expected results
Room temperature thermo-elastic case for vacuum-chamber tests	To derive the displacements of optical elements at room temperature with a fixed HSI platform, and with the thermal load as predicted during the operational case of TVAC tests. Heaters OFF.	Displacements of the optical elements will be used as a reference to adjust the optical model.
Hot thermo-elastic case for vacuum-chamber tests	To determine the maximum displacements of optical el- ements with a fixed HSI platform and thermal load as predicted by the hot operational case during TVAC tests. Heaters ON.	Larger displacements to be compared with tests and with the room temperature case.

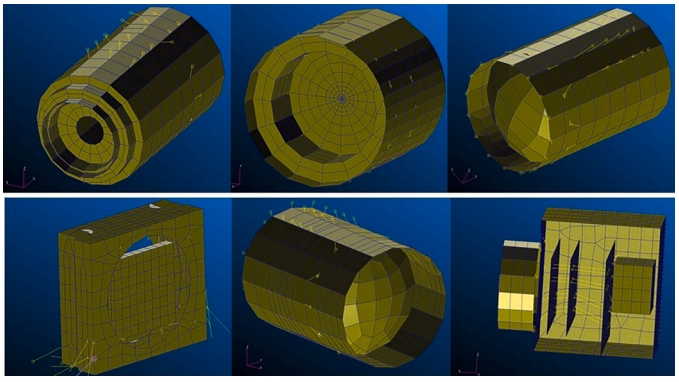

Fig. 12. Structural model of front objective (top left), slit assembly (top mid), collimator objective (top right), grating assembly (bottom left), detector objective (bottom mid), and sectioned detector box (bottom right). Yellow lines are the “handmade” joints to other HSI parts.

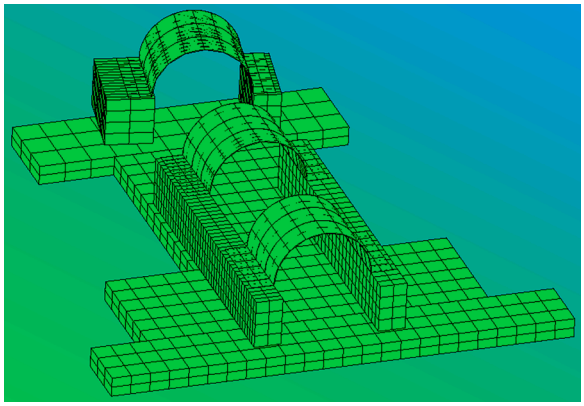

Fig. 13. Structural model of the HSI platform and brackets.

Prior to develop any thermo-elastic analyses, a series of checks shall be conducted on the structural models (refer to Table 3). Once these checks are all passed, the subsequent step involves mapping the temperatures onto the structural mesh using pySinas, which is based on the PAT method for their computation (refer to Table 4 to identify the reference cases). The PAT method rests on two assumptions. First, as the lumped pa- rameter method, it considers that the temperature from a thermal node corresponds to the average temperature of the related structural nodes. Furthermore, it assumes that heat conduction through the structural mesh fulfils to stationary heat diffusion in three dimensions.

Table 5
Materials properties employed in the structural model.

materials	density [kg/m^2]	elastic modulus [pa]	poisson ratio	cte·10^{-6} [m/m°c]
Fibre glass	2540	7.85e+10	0.22	5
Steel	4600	2.00E+11	0.285	12.2
Anodized Aluminium 6061	2700	6.90E+10	0.33	23.6
Anodized Aluminium 6082	2700	7.00E+10	0.33	24.0
Optical Glass	2560	6.63E+10	0.19	0.65
B270 Glass	2550	7.11E+10	0.22	8.6
H-LAFL5	3630	1.11E+11	0.283	5.5
H-ZF52	3530	9.60E+10	0.26	8.5
H-F4	2650	8.20E+10	0.228	7.8
H-ZLAF55D	4440	1.24E+11	0.293	6.2
H-FK61	2650	8.20E±10	0.228	7.8

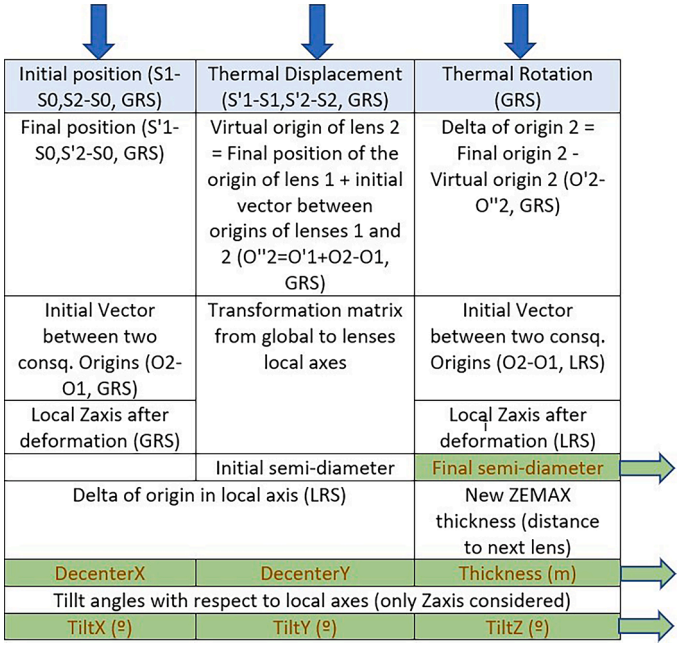

Fig. 14. Modelling process of the structural-optical interface. Outputs from NASTRAN are in blue, and required inputs for Zemax in green, with respect to the Global Reference System (GRS) and Local Reference System (LRS).

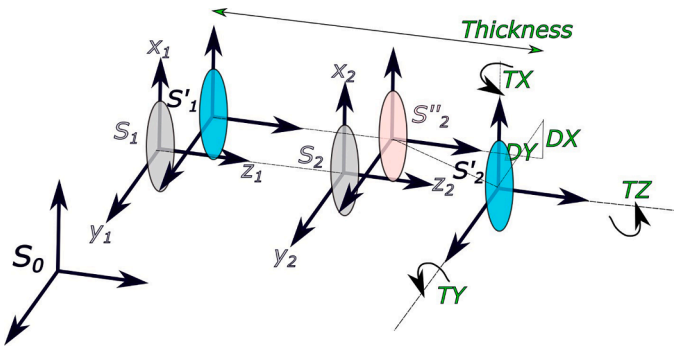

Fig. 15. Transformation scheme of reference systems between the structural and optical models for two consecutive lens. Inputs for Zemax in green. Initial position: S1 and S2; final position: S'1 and S'2; virtual position: S''2.

4.2. Description of the structural model

The structural model made for thermo-elastic analysis has several differences from the one made for dynamic structural analysis purposes. The primary discrepancy lies in the mesh resolution. In the structural model for dynamic analysis, this resolution must be refined enough to accurately capture nor- mal modes or stresses under static or dynamic loads. In con- trast, the mesh resolution for thermo-elastic analysis should be sufficiently detailed to encapsulate thermal gradients. Consequently, areas which are expected to have more significant thermal gradients should be assigned a higher mesh resolution. Here, a structural model with around 7000 nodes and 7000 ele- ments is developed.

Key components of the structural model are depicted in Figs. 12 and 13. This work focuses on integrating the structural model within the overarching thermo-elastic framework to en- hance our knowledge of the thermal effect on the optical per- formance of the system.

The materials employed in the structural model are listed in Table 5. The arrangement of these materials in the HSI parts is the same as in the thermal model elaborated in Section 3, with a reference temperature of 20 °C.

5. Optical model

To complete the thermo-elastic analysis chain towards the evaluation of the full STOP analysis, we have developed an optical model of the same hyperspectral camera in Zemax. Given that the objective of this work is to assess the impact of ther- mal deformations on the optical components, it is required to perform a preliminary stage of adapting the structural outputs from NASTRAN (explained in Section 5.1). Finally, the HSI optical model is described in Section 5.2.

5.1. Modelling process of the structure-optical interface

NASTRAN provides all displacements and rotations of the structural nodes in a global reference system. However, to feed the thermo-elastic response into Zemax for computing the lens de-centring and rotation, we require them to be defined rela- tive to each lens axis. The structure-optical interface process is illustrated in Fig. 14, with NASTRAN outputs highlighted in blue and the required Zemax inputs depicted in green. To streamline this calculation, we establish a local reference system at the centre of each lens and optical component in the structural model. In this local system, the Z axis points to the optical centre line, with the X axis representing the vertical di- rection and the Y axis the horizontal one.

The initial positions along with the final displacements and rotations of the points of these auxiliary coordinate frames are incorporated into an Excel file. This file performs several calculations including the computation of final coordinates, transformation matrix, final semi-diameter for each lens, the vari- ation of origin position and the tilt angles with respect to the local-to-lens reference system. A schematic representation of the transformation of reference systems between the structural and optical models for two consecutive lenses is provided in Fig. 15.

Given the large amount of lenses and optical components in the HSI, and subsequent deformation parameters, only the rigid-body displacements of the optics (as depicted in Fig. 14) are considered as inputs for the optical analysis in Zemax. While certain studies, such as the one conducted by [33], have focused on the comprehensive high-order analysis of the pri- mary optical component of a complete telescope, our instrument's optical components lack a distinct hierarchy. Therefore, a specific component has not been chosen for an in-depth in- vestigation, but all rigid body displacements and rotations are incorporated in the STOP analysis to identify most critical com- ponents.

Uncertainty exists in all input parameters, one being the tightening torque level of the bolts joining the platform to the brackets and the

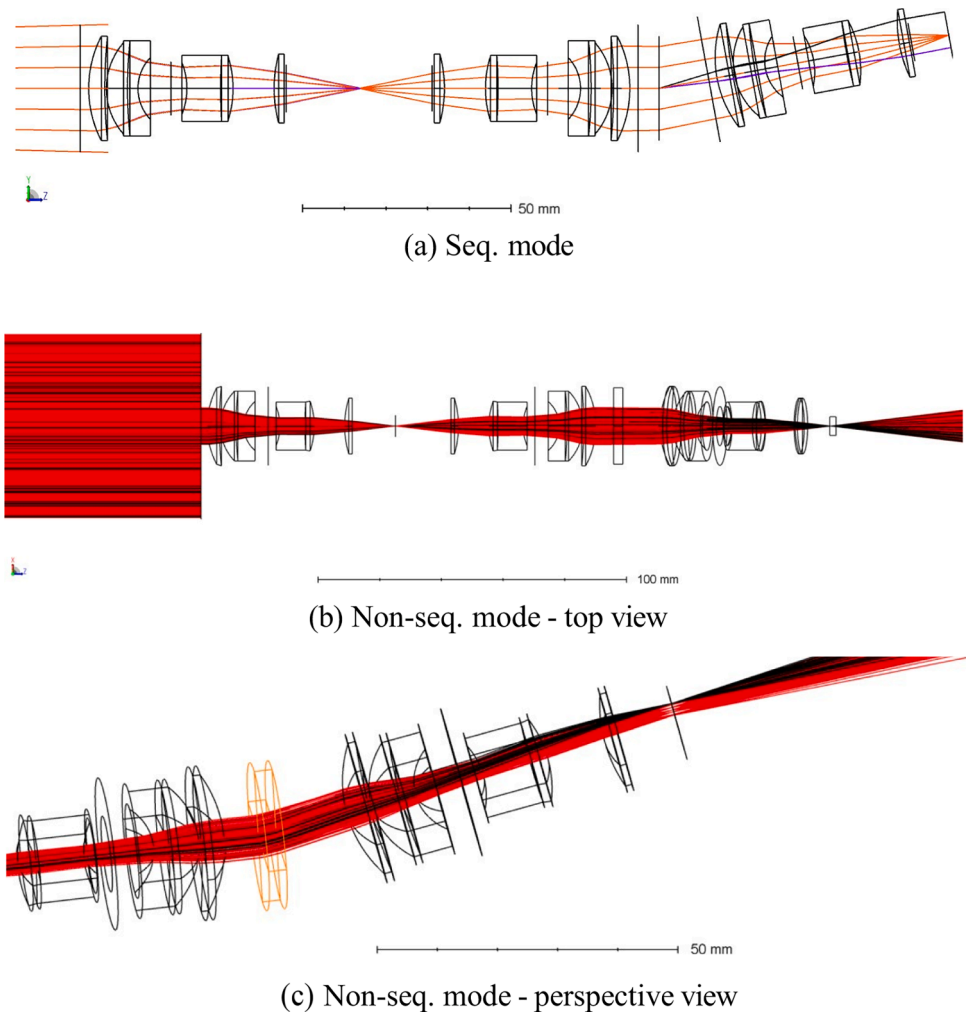

Fig. 16. Optical model views of the reference case: (a) Top view at the sequential mode; (b) Top view at non-sequential mode; (c) Perspective closer view of HSI after the slit at non-sequential mode.

brackets to the front and collimator objectives, thus needing from an experimental correlation with the structural model. The irradiance on the sensor for the main peaks of Argon light at cases between 0 and 32 W was used to fit an equivalent global CTE in the structural model, as described in the Section 5.2. This global CTE is a constant multiplier applied to all displacements and rotations of the lenses derived from NASTRAN.

5.2. Description of the optical model

An optical model is constructed to depict the optical performance of the HSI. The model, configured in Zemax OpticStudio, encompasses all the components above-mentioned: three lenses (objectives), a slit, a grating, and a detector, amounting to a total of 44 surfaces as shown in Fig. 16a. We model the light source in Zemax using a rectangle generator of light rays, adjusting some of the irradiation peaks to match the wavelength of pure Argon light peaks, set within the 695 to 842 nm range, for the thermal case of 23 °C. The specific single Argon peaks in this range are chosen to be modelled, because they appear as single separated peaks by the instrument [34]. This is to prevent using overlapping peaks in the analysis when measuring with a spectral resolution of about 5 nm.

The optical diagram is followed as shown in Fig. 1. The front lens receives and focuses the incoming light onto the slit. The slit serves as a spatial filter, allowing only the rays in the optical model global-X axis, the spatial strip captured by the HSI, to pass. The collimator lens configuration, a mirror image of the front lens configuration, directs these rays to run parallel to each other. Subsequently, these parallel rays are diffracted by the grating, splitting them according to wavelength. The grating, modelled in Zemax with two breakpoints for setting the incident and diffracting angles, features a diffracting surface with 0.3 lines per μm. Finally, the detector objective lens gathers rays of the same wavelength and focuses them at specific positions along the detector.

In the nominal design configuration at reference temperature, the axes of the front and detector objectives lenses align with the 595.5 nm ray in the optical model Y-Z plane, both before and after the grating position. Additionally, the detector is positioned such that the 595.5 nm ray targets the centre of the detector within the X-Y plane. The limiting wavelength range, established via the Zemax sequential model (see Fig. 16a), is set between 405 nm (lower limit due to the grating's minimum diffracted angle) and 960.7 nm (upper limit due to the geomet- ric edge of the detector). Following the limiting wavelength fitting with the sequential optical model, the model is transitioned to the non-sequential mode for effective ray tracing from the light source to the detector, thus enabling the computation of light irradiance distribution with respect to wavelength (see Fig. 16b and c). In the sequential mode, rays are traced from the light source to the detector, following the order of the lenses along the light path. It is simpler, and numerically fast. Non-sequential means that the rays trace in the actual physical order they hit various objects and surfaces, which may not be in the sequential order that the surfaces are defined. Rays in a non-sequential trace may hit the same object repeatedly, and entirely miss other objects. The order in which

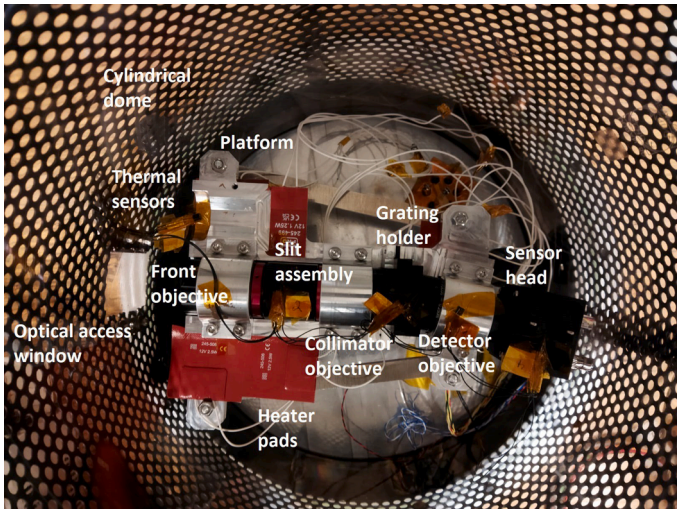

Fig. 17. HSI inside the TVAC, with temperature sensors and heater pads for thermal control. An optical access window is available.

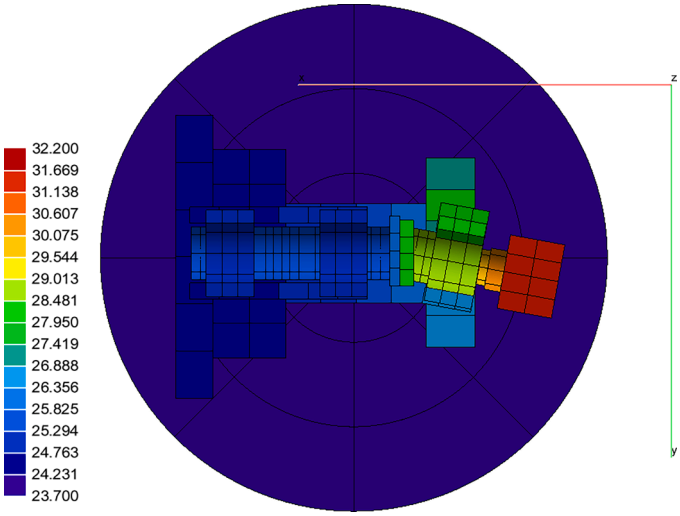

Fig. 18. Temperature map calculated with the TMM. Heating power = 0 W. HSI ON.

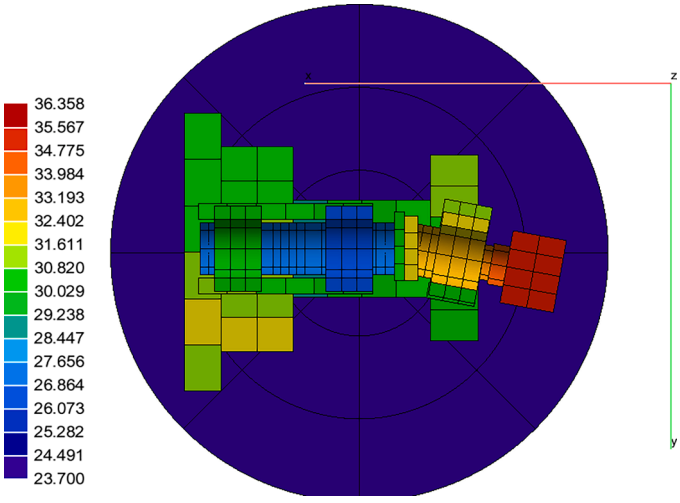

Fig. 19. Temperature map calculated with the TMM. Heating power = 8 W. HSI ON.

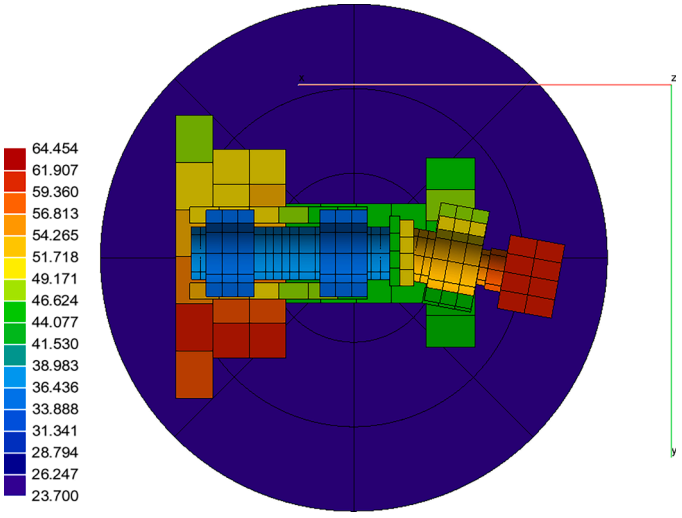

Fig. 20. Temperature map calculated with the TMM. Heating power = 32 W. HSI ON.

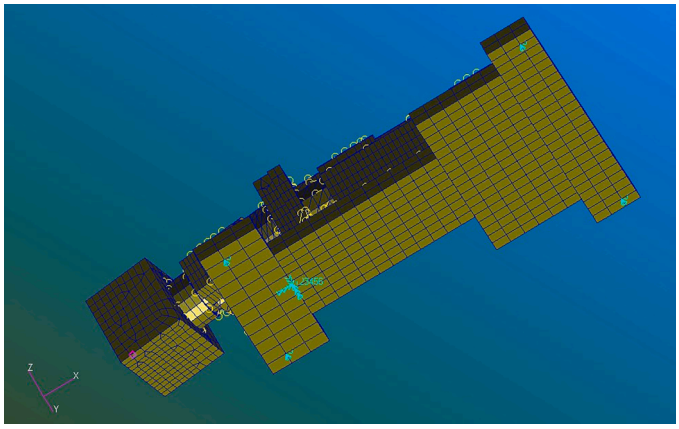

Fig. 21. Boundary conditions for the structural model. The calculated centre of gravity is fixed in the 6 degrees of freedom. Additionally, the vertical displacement of the joints to rods are fixed.

rays hit the objects can be different for each ray, and depends upon the object geometry and the angle and position of the rays.

We account for the impact of temperature variation in Zemax through geometric transformations derived from thermo-structural simulations, and we do not set the environmental values of Zemax differently. This way we avoid modifying the temperature twice. In the optical model fitting at reference tem- perature at 23 °C, modifications of the theoretical optical model (in terms of position and tilts of some lenses) were required. We did this to align the focused peak formation with the focused peaks that we achieved in the experimental set-up, see the Section 6. In the optical model the reference 23 °C set up is determined, by aligning the peaks to the experimentally found peaks. From the structural model the tilt and decentring of each component is determined for the new temperatures (33 °C, 50 °C). Then a correction is made for the tilt and decentring of the peaks with the C factor chosen such that the height of intensity peaks are in proximity with the experimental findings for the peaks at the reference temperature. Therefore, the new tilt and position after correcting with C (pos_C and $tilt_C$) of the components are calculated as follows,

$$pos_C = pos_{23} + \frac{pos50 - pos23}{C} \tag{1}$$

where pos_{50} is the position at the new temperature (50 °C or 33 °C). For

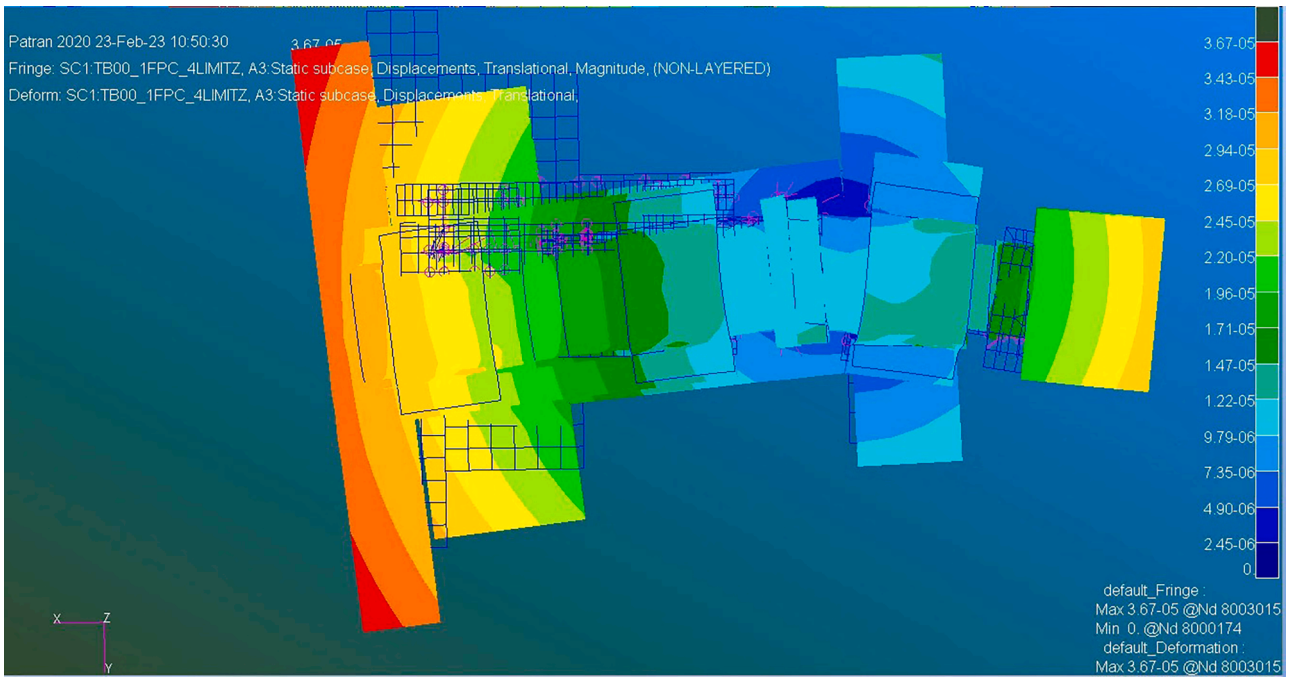

Fig. 22. Displacement map calculated with the structural model. Heating power = 0 W. HSI ON.

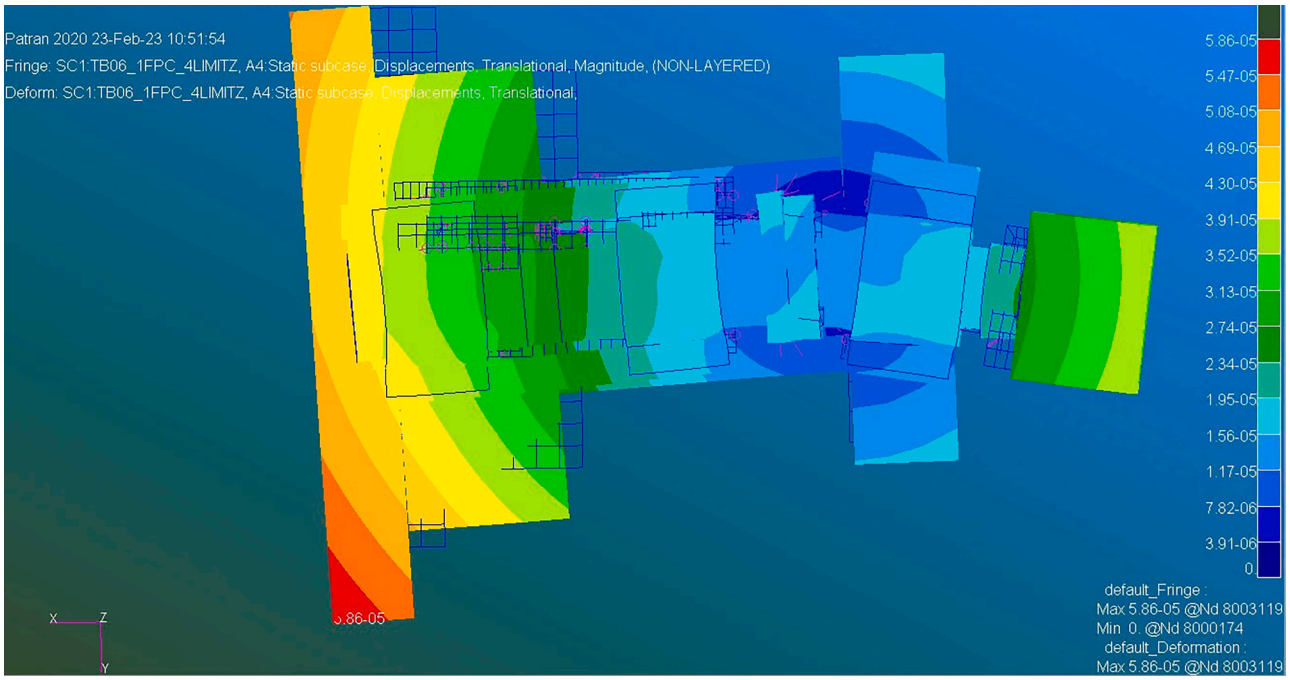

Fig. 23. Displacement map calculated with the structural model. Heating power = 8 W. HSI ON.

the tilt the same equation is applied but then *pos* is replaced with *tilt*. This is done because the structural model is not fitted, and there are uncertainties caused by, for example, the tightening pressure in the bolts from the objectives to the baseplate. The factor C is chosen so that the height of the intensity peaks of the optical model matches with the height of intensity of experimental measurements of the similar peaks at the temperature of 50 °C. In the experiments a shift of the peaks to higher wavelengths was observed for the measurements of 50 °C, this is caused by a movement of the lamp set-up during the experiments and this is explained in more detail in [35], for completeness this result is also shown in Fig. 25. In this analysis, the indices of the 50 °C are assumed to be at the same location as for the 23 and 33 °C. These adjustments are justified in the context of this research considering that the HSI is a low-cost, Commercial Off-The-Shelf (COTS) system and minor deviations from the design are plausible. For instance, the theoretical central wavelength was expected to be 600 nm, but the actual setup aligned at 595.5 nm. In the discussion sec- tion, we could consider improvements to further refine the optical model and better align it with the experiments.

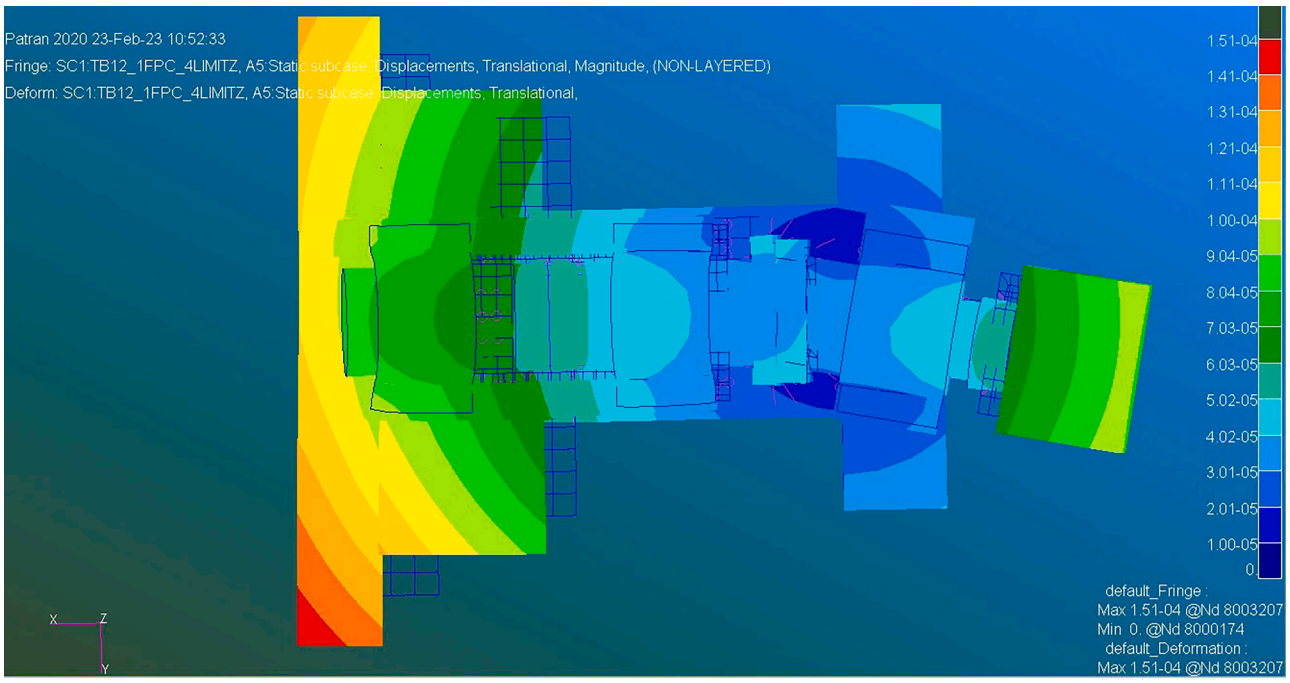

Fig. 24. Displacement map calculated with the structural model. Heating power = 32 W. HSI ON.

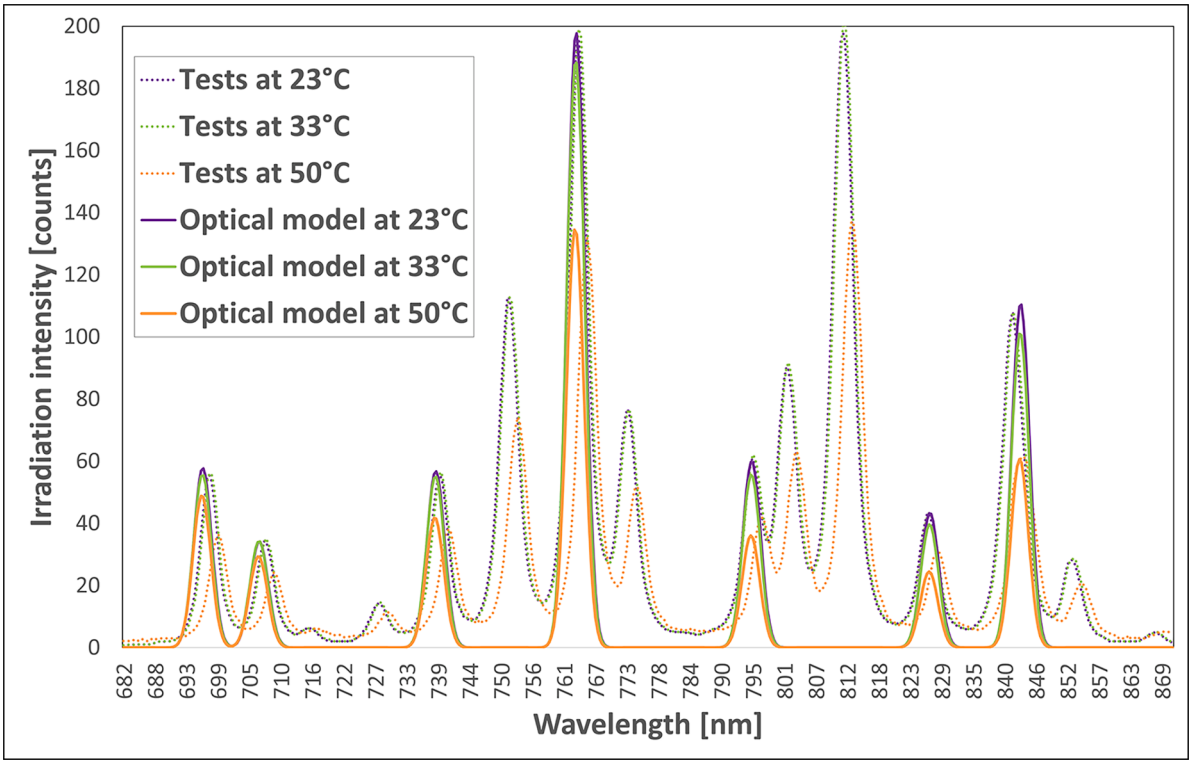

Fig. 25. Intensity variation with wavelength [nm] for tests and optical model at 23, 33, and 50 °C.

6. Experimental set-up

NTNU has developed a custom TVAC for testing under vacuum conditions. The chamber achieves a pressure below 0.5E- 4 mbar, providing a sufficiently high vacuum level for assessing the performance of the hyperspectral camera under vacuum conditions. As depicted in Fig. 17, the HSI performance was evaluated within this TVAC.

The chamber walls includes an electrical feedthrough for heater pads and a cross feedthrough for several elements, including the ethernet cable, temperature sensors, the HSI power supply, and a pressure sensor. In addition, the chamber features an optical access window in front of the front lens and an infrared-transparent access point in the chamber's top plate.

To manage thermal Device Under Test (DUT) within the TVAC, we use an infrared camera with a spectral range between 8 and 14 μm for temperature mapping, five temperature sensors for point-specific

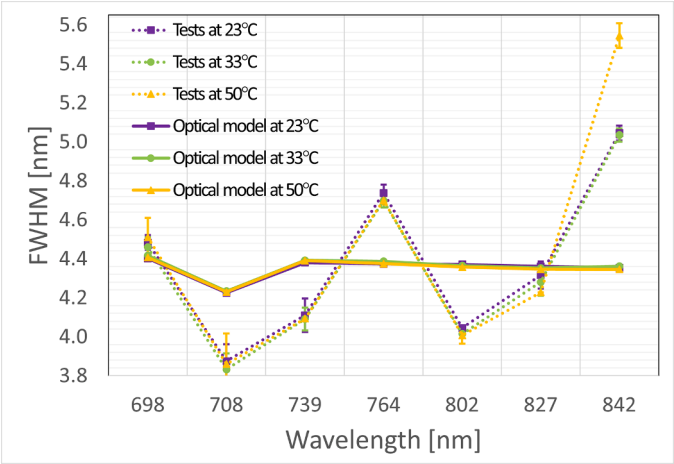

Fig. 26. FWHM for the main peaks of Argon light calculated from the test results and the Zemax simulations. Standard deviation for 10 captures during each test case.

measurements, and heater pads for warming the DUT platform.

The performance of the HSI is measured at three distinct thermal cases, corresponding to heater pad power levels of 0, 8, and 32 W. These levels induced three individual temperature conditions on the HSI platform: 23, 33, and 50 °C. The case of 0 W power was used to adjust the width and height of Argon peaks in the optical model, while the 0 and 32 W cases were used for fitting the relative displacements in the structural model as above mentioned. Lastly, all the cases were employed to correlate the temperatures in the thermal model.

7. Results and discussion

In this section, we present the results derived from the thermal, structural, and optical models. We consider three different scenarios, each representing a specific temperature environment, to assess the variability of irradiance intensity with temperature and wavelength. As explained before, the temperature maps for these scenarios corresponds to heating power levels of 0, 8, and 32 W, and are depicted in Figs. 18–20, respectively.

The structural model is used to calculate node displacements under the same thermal loads. The boundary conditions for the HSI platform within the CubeSat consist of four damper supports linked to the CubeSat structure, which were replicated in tests using supporting rods that allow horizontal movement but constraints the vertical displacements. In the structural model, the rigid solid motion is restricted by fixing a single node, easing the calculation of relative displacements between deformated points. In essence, the thermo-elastic study disregards rigid body movements. Furthermore, the vertical displacements of the HSI platform where the rods cross the structure were con-strained, as illustrated in Fig. 21.

Figs. 22–24 show the displacement maps for heating power levels of 0, 8, and 32 W, respectively. It is remarkable that the displacement pattern remains quasi invariant, with only the translational modulus increasing with temperature. The maximal displacements measured are 0.037, 0.059, and 0.151 mm, respectively. There exist also a small variation with temperature of the orientation of the front part of the platform.

Moving on to the optical model, we first present the spectral distribution of intensity (expressed in counts per 8 sensor bits) in Fig. 25. As explained in Section 5.2, the positioning and tilting of each object in the optical train is chosen such that the height of intensity peaks are in close proximity of experimental results, at the reference temperatures for the structural and optical models. Therefore, similar as to the experimental results, a reduction in intensity with increased temperature in the optical model can be seen. This possibly is caused by the sig- nificant deformation of numerous lenses and optical elements. In addition, the FWHM for each peak is determined from simulations, and plotted in the same Fig. 26 as the FWHM coming from the experiments. The standard deviation is also shown for each peak, which is calculated by using 10 consecutive captures taken with the HSI. It can be observed that the standard devi- ation is relatively small, so the repeatability of HSI images for each temperature is demonstrated. The FWHM variation with temperature along the Argon light peaks is modelled consistent in the Zemax model than in experimental results. The priority was that the average value is fairly similar between both tests and simulations. In all cases, the FWHM value is close but bigger than the theoretical HSI designed value of 3.3 nm, and similar to the FWHM of 5 nm found for the HSI flight model that is currently in orbit [20]. For Argon light, some peaks, like the peak at 842 nm, are really part of a merged double peak at 841–842 nm. Thus, in the tests we can see an increase of the FWHM. However, in the Zemax model there is no so much variation of the FWHM due to merged peaks because each light source peak is an input at

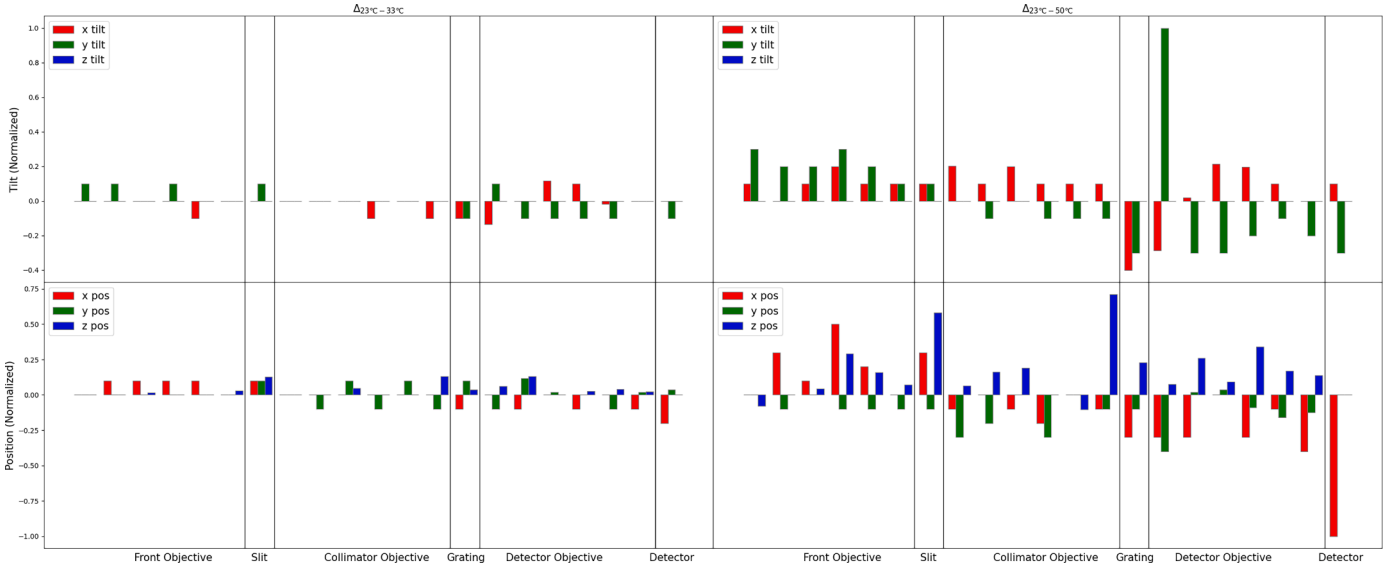

Fig. 27. The tilt and displacement in the x, y, and z direction of the optics model because of the temperature change. For each larger objective, with the detailed lenses.

a unique frequency.

The normalized changes in position and tilt of each compo- nent are determined and can be seen for each object number, and for two temperature differences (23 °C and 33 °C, and 23 °C and 50 °C) in Fig. 27. The definitions for the x-, y- and z- directions in the optical model (OM) can be seen in Fig. 16. It should be remarked that structural and optical reference systems are different, according to Figs. 21 and 16, respectively. Overall it can be seen that the positions and tilts mostly change with a higher temperature difference. The largest change in the tilt is 0.01°, and in position 0.002 mm. In Fig. 27 no tilt in the optical model z-direction can be seen. This is because in the boundary conditions we are fixing the vertical displacements of the joint points in the threaded rods. This is preventing tilts to occur in the global structural model X-direction (see Fig. 21), equivalent to the global optical model Z-direction. The largest tilt can be seen in the first lens of detector objective, in the OM y-direction. The largest change in position can be seen in the OM x-direction for the detector (23 °C–50 °C). This can be explained by the requirement that we set that the FWHM remains stable in setting up the model. In the experiments we see larger deviations in the FWHM, which is expected because the HSI is focused on the central wavelength, and the further on the detector from the central wavelength, the lower the spectral res- olution would be. This means that the detector in the model is set such that the signal is in this uniform focus over this region.

The heating pads in the experimental set up were located under the platform around the front objective, slit, and collimator objective. Therefore, they induce thermal deformation in the complete platform that moves the HSI objectives. Even though the objectives used in the set-up are identical, it can be seen from the results that the position of the objective (and lenses) determines whether a tilt or position shift can be expected, rather then that there is one lens that is most sensitive for displacement.

8. Conclusions

Analysing the performance of optical instruments on satellites is a complex task, which requires an integrated evaluation of the thermal, structural, and optical models. This complexity often results in significant costs, making such analysis less feasible for small satellite projects. Specifically, thermo-elastic lens deformations can considerably affect the efficiency of optical instruments, particularly hyperspectral cameras.

In order to validate the application of the STOP analysis chain to the HYPSO HSI model, we performed a test campaign. This involved applying identical thermal loads to both the HSI STOP numerical models and the HSI engineering model within a TVAC. We then compared the numerical and experimental optical outputs, using thermocouples and an infrared camera to profile the thermal loads, and employing the FWHM metric to assess the thermal performance of the HSI.

The temperature maps derived from the thermal model for three thermal scenarios were subsequently adjusted to align with the measurements from the thermocouples and an infrared imager, obtained during TVAC tests. Subsequent structural thermo-elastic analysis revealed a clear linear relationship between thermal deformation and temperature.

After adjusting the optical model to fit the reference thermal case by a correction to the height of intensity peaks, we determined the displacements and tilts of each component in the model. We find that a larger temperature differences causes more shifts and tilts. Within the objective that is three times used in the optical set up, it is not found that one lens is more sensitive to tilts and displacements than other lenses. We have confidence in the models because we have correlated it with the experimental tests. We conclude that this STOP analysis method can be a tool to identify critical optical components in remote sensing applications. The next step is to apply thermal test cases in orbit.

In conclusion, we have employed a hybrid numerical-test method to characterize the STOP performance of a hyperspectral camera under space conditions. This novel methodology, proving successful in its initial application, holds promise for future implementations in successive HYPSO generations and other cost-effective small satellite projects, aimed to Earth remote sensing or astronomical observations.

Declarations

Funding

This work was supported by the Research Council of Norway through the Centre of Excellence funding scheme (NTNU- AMOS, grant no. 223,254) and the projects MASSIVE (grant no. 270,959) and HYPSCI (grant no. 325,961), and the Norwe- gian Space Agency and the European Space Agency through PRODEX (no. 4,000,132,515). Besides, the researcher Fermin Navarro Medina received a research grant by Spanish Ministry of Universities within the "Jose Castillejo" program of mobility stays abroad for young PhDs with reference number CAS21/00,502, to stay in NTNU in Trondheim (Norway).

Author contributions

All authors contributed to the study conception and design. Material preparation, data collection and analysis were performed by [Adriënne Esmeralda Oudijk] and [Fermin Navarro-Medina]. The thermal model and analysis and the thermal-structural interface were performed by [Uxia Garcia-Luis] and [Fermin Navarro-Medina]. The structural model and analysis and the structural-optical interface were performed by [Alejandro Gomez-San-Juan] and [Fermin Navarro-Medina]. The optical model and analysis, and the experiments were performed by [Adriënne Esmeralda Oudijk], [Fermin Navarro-Medina] and [Marie Bøe Henriksen]. The first draft of the manuscript was written by [Fermin Navarro-Medina] and [Adriënne Esmeralda Oudijk] and all authors commented on previous versions of the manuscript. The final edition of the text and of all figures was done by [Uxia Garcia-Luis]. All authors read and approved the final manuscript.

Declaration of generative AI and AI-assisted technologies in the writing process

During the preparation of this work the authors used GPT-4 in order to improve language and readability. After using this tool, the authors reviewed and edited the content as needed and take full responsibility for the content of the publication.

Declaration of Competing Interest

The authors declare the following financial interests/personal relationships which may be considered as potential competing interests:

Fermin Navarro-Medina reports financial support was provided by Spanish Ministry of Universities.

Data availability

Data will be made available on request.

References

[1] Nie R, He B, Yan S, Ma X. Optimization design method for the cable network of mesh reflector antennas considering space thermal effects. Aerosp Sci Technol 2019;94. https://doi.org/10.1016/j.ast.2019.105380.

[2] Lu GY, Zhou JY, Cai GP, Fang GQ, Lv LL, Peng FJ. Studies of thermal deformation and shape control of a space planar phased array antenna. Aerosp Sci Technol 2019;93. https://doi.org/10.1016/j.ast.2019.105311.

[3] Thornton E. Thermal structures for aerospace applications. 1st Edition. American Institute of Aeronautics and Astronautics; 1996.

[4] Appel S, Wijker J. Simulation of thermoelastic behaviour of spacecraft structures. 1st Edition. Srpinger International Publishing; 2021.

[5] M. Koot, S. Apple, S. Simonian, Temperature mapping for structural thermoelastic analysis; method benchmarking., European conference on spacecraft structures, materials mechanical testing, 2018.
[6] TEC-MESA/ESTEC European guidelines for thermo-elastic verification (stm-285). 1st ed. Noordwijk: ESA Communications; 2023. https://www.esa.int/About_Us/ESA_Publications/STM-285_European_Guidelines_for_Thermo-Elastic_Verification).
[7] Johnston J. Integrated modeling activities for the james webb space telescope: structural-thermal-optical analysis. Proc SPIE Int Soc Opt Eng 2004;5487:600–10.
[8] Tse L, Chang Z, Slimko E, Somawardhana R. Structural, thermal, and optical performance (STOP) modeling and analysis for surface water and ocean topography mission. In: Proceedings of the 48th international conference on environmental systems; 2018.
[9] Garcia-Perez A, Alonso G, Gomez-San-Juan A, Perez Alvarez J. Thermoelastic evaluation of the payload module of the ARIEL mission. Exp Astron 2022;53:831–46. https://doi.org/10.1007/s10686-021-09704-0.
[10] Heesel E, Weigel T, Lochmatter P, Grond ER. Coupled thermo- elastic and optical performance analyses of a reflective baffle for the BepiColombo laser altimeter (BELA) receiver. In: Proceedings of the international conference on space optics ICSO; 2008. https://doi.org/10.1117/12.2308252.
[11] Dipasquale D, Debei S, Cremonese G, Capaccioni F, Palumbo P. Optical performance evaluation of the high spatial resolution imaging camera of BepiColombo space mission. Opt Laser Technol 2021;141. https://doi.org/10.1016/j.optlastec.2021.107172.
[12] Jin H, Lim J, Kim Y, Kim S. Optical design of a reflecting telescope for CubeSat. J Opt Soc Korea 2013;17(6):533–7.
[13] Muller DEA. The solar orbiter mission. Astron Astrophys 2020;642(A1). https://doi.org/10.1051/0004-6361/202038467.
[14] Herceg M, Jorgensen P, Jorgense J. Thermoelastic response of the juno spacecraft's solar array/magnetometer boom and its applicability to improved magnetic field investigation. Earth Space Sci 2020. https://doi.org/10.1029/2020EA001338.
[15] Givoli D, Rand O. Harmonic finite-element thermoelastic analysis of space frames and trusses. J Therm Stress 1993;16(3). https://doi.org/10.1080/01495739308946228.
[16] Svendsen S. Simulating the effects of thermoelastic deformation on the THESEUS soft x-ray imager optics. Proc SPIE 2019;111191R. (https://www.spiedigitallibrary.org/conference-proceedings-of-spie/11119/2529113/Simulating-the-effects-of-thermoelastic-deformation-on-the-THESEUS-Soft/10.1117/12.2529113.full).
[17] Prentice E, Grøtte M, Sigernes F, Johansen TA. Design of hyperspectral imager using cots optics for small satellite applications. In: Proceedings of the international conference on space optics ICSO; 2021.
[18] Henriksen MB, Prentice EF, van Hazendonk CM, Sigernes F, Johansen TA. A do-it-yourself VIS/NIR pushbroom hyperspectral imager with C-mount optics. Opt Contin 2022;1:427–41.
[19] Henriksen MB, Prentice EF, Sigernes F, Johansen TA. Pre launch calibration of the HYPSO-1 CubeSat hyperspectral payload. IEEE Aerospace Conference; 2022.
[20] Bakken S, Henriksen MB, Birkeland R, Langer DD, Oudijk AE, Berg S, Pursley Y, Garrett JL, Gran-Jansen F, Honoré-Livermore E, et al. HYPSO-1 CubeSat: first images and in-orbit characterization. Remote Sens 2023;15(3):755.
[21] Baussart P, D'Amico J, Behar Lafenetre S, de Cillia M, Laine B, Sablerolle S, Ertel H, Vaughan M, Perachino L. Thermo elastic test campaign in the frame of ESA activity 'i-meter. ECSSMET 2021.
[22] Torkildsen HE, Skauli T. Measurement of point spread function for characterization of coregistration and resolution: comparison of two commercial hyperspectral cameras. Algorithms and technologies for multispectral, hyperspectral, and ultraspectral imagery XXIV, 10644. International Society for Optics and Photonics; 2018, 106441F.
[23] Ali A, Tong J, Ali H, Mughal MR, Reyneri LM. A detailed thermal and effective induced residual spin rate analysis for LEO small satellites. IEEE Access 2020;8:146196–207.
[24] Garzoń A, Villanueva YA. Thermal analysis of satellite libertad 2: a guide to CubeSat temperature prediction. J Aerosp Technol Manag 2018;10.
[25] Richter S. STOP analysis for a spacecraft camera distortion model i. abstract. https://sioslab.com/wp-content/uploads/2021/06/Richter_-Sarah_MEng-2021_Final_Report.pdf.
[26] Pérez-Grande I, Sanz-Andrés A, Guerra C, Alonso G. Analytical study of the thermal behaviour and stability of a small satellite. Appl Therm Eng 2009;29(11–12):2567–73.
[27] Anvari A, Farhani F, Niaki K. Comparative study on space qualified paints used for thermal control of a small satellite. Iran J Chem Eng 2009;6(2):2009 (Spring), IAChE.
[28] Cubas J, Gomez-San-Juan AM, Pindado S. On the thermo-electric modelling of smallsats. In: Proceedings of the International Conference on Environmental Systems; 2020.
[29] Prentice E, Henriksen M, Johansen T, Navarro-Medina F, San Juan A. Characterizing spectral response in thermal enviornments, the HYPSO-1 hyperspectral imager. IEEE Aerosp Conf (AERO) 2022. https://doi.org/10.1109/AERO53065.2022.9843389.
[30] Prentice EF, Honoré-Livermore E, Bakken S, Henriksen MB, Birkeland R, Hjertenæs M, et al. Pre-launch assembly, integration, and testing strategy of a hyperspectral imaging CubeSat, HYPSO 1. Remote Sens 2022;14:4584.
[31] Gilmore D. Spacecraft thermal control handbook. 1st Edition. Fundamental Technologies, The Aerospace Corporation Press; 2002. Vol. I.
[32] Schott, Schott optical glass collection datasheets (2018). URL https://www.schott.com/en-gb/products/optical-glass-p1000267/downloads (last access at 05/02/2023).
[33] Borden M, Lewis D, Ochoa H, Jones-Wilson L, Susca S, Porter M, Massey R, Clark P, Netterfield B. Thermal, structural, and optical analysis of a balloon-based imaging system. Astron Soc Pac 2017;129(973). https://doi.org/10.1088/1538-3873/129/973/035001.
[34] Henriksen MB, Sigernes F, Johansen TA. A closer look at a spec- trographic wavelength calibration. In: Proceedings of the 12th workshop on hyperspectral imaging and signal processing: evolution in remote sensing (WHISPERS). IEEE; 2022. p. 1–5.
[35] Navarro-Medina F, Oudijk AE, Henriksen MB, Gjersvik A, Grønvold FS, Johansen TA. Experimental set-up of a thermal vacuum chamber for thermal model in-house correlation and characterization of the HYPSO hyperspectral imager. CEAS Space J 2023. https://doi.org/10.1007/s12567-023-00501-3.